

Article

Non-Thermal Plasma-Modified Ru-Sn-Ti Catalyst for Chlorinated Volatile Organic Compound Degradation

Yujie Fu ¹, You Zhang ², Qi Xin ¹, Zhong Zheng ¹, Yu Zhang ¹, Yang Yang ^{1,*},
Shaojun Liu ¹ , Xiao Zhang ¹, Chenghang Zheng ¹ and Xiang Gao ^{1,*}

¹ Institute for Thermal Power Engineering, Zhejiang University, Hangzhou 310007, China; fuyjacky@zju.edu.cn (Y.F.); 11627064@zju.edu.cn (Q.X.); 21927034@zju.edu.cn (Z.Z.); carrie_z@zju.edu.cn (Y.Z.); phoenix205@zju.edu.cn (S.L.); zhangx_energy@zju.edu.cn (X.Z.); zhengch2003@zju.edu.cn (C.Z.)

² Zhejiang University Energy Engineering Design and Research Institute Co., LTD, Hangzhou 310007, China; 164152269@zju.edu.cn

* Correspondence: Y_Yawn@zju.edu.cn (Y.Y.); xgao1@zju.edu.cn (X.G.); Tel.: +86-18058430908 (Y.Y.)

Received: 13 October 2020; Accepted: 20 November 2020; Published: 13 December 2020



Abstract: Chlorinated volatile organic compounds (CVOCs) are vital environmental concerns due to their low biodegradability and long-term persistence. Catalytic combustion technology is one of the more commonly used technologies for the treatment of CVOCs. Catalysts with high low-temperature activity, superior selectivity of non-toxic products, and resistance to chlorine poisoning are desirable. Here we adopted a plasma treatment method to synthesize a tin-doped titania loaded with ruthenium dioxide (RuO₂) catalyst, possessing enhanced activity ($T_{90\%}$, the temperature at which 90% of dichloromethane (DCM) is decomposed, is 262 °C) compared to the catalyst prepared by the conventional calcination method. As revealed by transmission electron microscopy, X-ray diffraction, N₂ adsorption, X-ray photoelectron spectroscopy, and hydrogen temperature-programmed reduction, the high surface area of the tin-doped titania catalyst and the enhanced dispersion and surface oxidation of RuO₂ induced by plasma treatment were found to be the main factors determining excellent catalytic activities.

Keywords: nonthermal plasma; ruthenium; titania; CVOCs degradation

1. Introduction

Chlorinated volatile organic compounds (CVOCs), such as dichloromethane (DCM), chlorobenzene (CB) and dichloroethylene (DCE), are considered to be extremely toxic pollutants due to their high carcinogenicity, low biodegradability, and long-term persistence [1–4]. CVOCs are widely used in detergent, degreasant, chemical extractant, and paint additive, and contribute to the formation of tropospheric ozone, photochemical smog, and haze [5–8]. Consequently, versatile methods have been developed to reduce their environmental impacts, including adsorption recovery [9], photothermal decomposition [10], direct thermal combustion [11], and catalytic combustion [12,13]. Among them, catalytic combustion is considered to be a promising technique due to its high activity, high selectivity, good stability, and low energy consumption. Recently, transition metal oxides loaded with noble metal oxides have gained wide attention due to their high catalytic activities, superb resistance against chlorine-poisoning, and strong stability [14–16]. However, the catalysts synthesized by the conventional calcination method were reported to lack oxidation activity in low temperatures. The calcination process often led to the aggregation of particles, over-growth of crystalline, and pore collapse, which finally lowered the efficiency of pollutant decomposition [13]. It has been reported that the particle size and

surface area of catalysts [17], the dispersion of active components on support [18], and the oxidation state of the active sites [19], are the critical factors controlling the activities.

Non-thermal plasma (NTP) has been widely applied in surface modification [20–23], offering the advantages of room-temperature operation and non-equilibrium processes. In catalyst preparation, NTP could transform the precursor into oxide and simultaneously avoid the loss of activity caused by the high-temperature conditions in conventional calcination methods [24–26]. During the NTP process, the generated energetic clusters and active radicals are capable of dispersing precursors into smaller particles and inducing the active sites to higher oxidation states. This process makes NTP treatment an efficient strategy for the morphology reconstruction of catalysts with higher porosity. More importantly, the low-temperature feature of NTP treatment could avoid the particle aggregation [27,28], crystal sublimation, crystal growth [29,30] and pore collapse issues [31,32], which were inevitable in conventional calcination methods.

TiO₂ was widely surveyed for its low cost and stability in the reaction atmosphere, while the rutile phase had great chemical reactive activity [33,34]. It was previously found that tin-doped titanium dioxide (Sn-TiO₂) loaded with ruthenium dioxide (RuO₂), which was dominated with rutile phase, showed excellent catalytic activities at high temperatures (>350 °C) in the oxidative removal of DCM, with high carbon dioxide (CO₂) selectivity and strong stability under HCl/Cl-containing atmosphere [14,35]. The loading of RuO₂ would induce the Cl to be mainly converted to Cl₂ with poor adsorption on the active sites [18]. Nonetheless, this kind of catalyst still suffers from insufficient low-temperature activity and particle agglomeration.

In the present work, non-thermal plasma treatment is employed for the preparation of RuO₂/SnTiO₂ catalysts, exhibiting enhanced DCM oxidation activities compared to the calcined counterpart. To understand the promotional effects triggered by plasma treatment, hydrogen temperature-programmed reduction, X-ray diffraction, X-ray photoelectron spectroscopy (XPS), and CO pulse chemisorption were conducted on the catalysts. The increased specific surface area and oxidation activity induced by the NTP treatment were found to be the origins of the enhanced catalytic performance.

2. Results

2.1. Catalytic Performance Evaluation

Sn-TiO₂ solid solutions were prepared via the co-precipitation method, and RuO₂ was loaded by the dipping method to gain Ru-SnTiO₂ (denoted as RST). The RST samples were respectively treated by plasma atmosphere with 20% O₂ (denoted as RST-P) and by calcination at 550 °C for 5 h in air (denoted as RST-C). The catalytic performance of the samples was evaluated in a quartz tube reactor. The reactive atmosphere was under 1000 ppm DCM, 20% O₂ and balanced rest with N₂. The DCM oxidation activity over the RuO₂/Sn_{0.2}Ti_{0.8}O₂ catalysts, which were prepared by thermal calcination treatment (RST-C) or by plasma treatment (RST-P), was surveyed and the results are demonstrated in Figure 1a. It can be found that the catalytic activity of RST-P (T_{90%} was 262 °C) was significantly higher than that of RST-C (T_{90%} was 299 °C). RST-P also possessed good stability without perceivable deactivation for 24 h at 250 and 275 °C (Figure 1c). Furthermore, RST-P had a greater oxidation activity in low temperature, and its DCM conversion rate increased from 25.9% to 48.1% at 200 °C. These results indicated that air-plasma treatment is beneficial for the enhancement of catalytic activity. Figure 1b shows the selectivity of CO₂ from DCM oxidation over different samples. According to the carbon equilibrium before and after reaction, the more DCM is converted to CO₂, the less toxic the organic byproducts that are produced. It was shown that the selectivity of CO₂ was significantly improved with plasma treatment compared to the calcined counterpart, especially at temperatures lower than 250 °C. The DCM conversion rate reached 90%, with the corresponding selectivity of CO₂ above 90%, at 275 °C. These results showed the promotional effects of plasma for DCM oxidation activity.

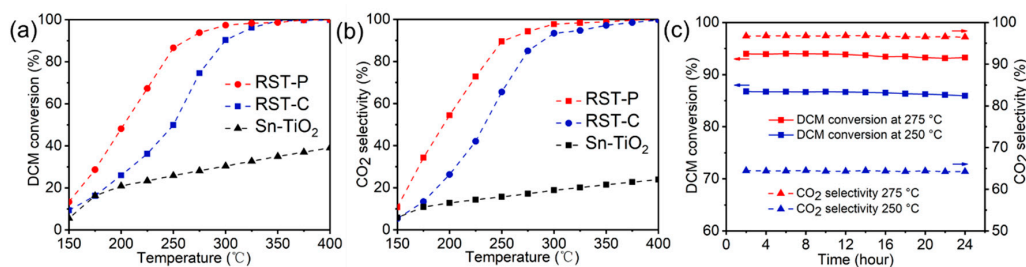


Figure 1. Catalytic performance of DCM oxidation by different synthesis methods: (a) DCM conversion, (b) selectivity of CO₂, (c) stability test for RST-P at 250 °C and 275 °C.

2.2. Catalyst Morphology and Crystallinity

To understand the effects of plasma treatment on the catalytic activities of the RST catalysts, the catalyst morphology and crystallinity were characterized. The surface area estimated by BET method and the pore properties of the two samples are shown in Table 1. It was shown that the specific surface area of the plasma-treated sample increased to 46.807 m²/g (37.397 m²/g with RST-C). The high specific surface area favored the exposure of more active sites to improve the catalytic activities of DCM oxidation [36–39]. It was proposed that the plasma preferred to discharge near the inner walls of pores [40,41], destroying the original pore structure and sequentially reconstructing it, resulting in the increase of specific surface area with almost the same total pore volume. High porosity promotes the accessibility of active sites, and facilitates the contact between DCM molecules and the surface active sites, enhancing the oxidation of DCM.

Table 1. Specific surface area and pore properties of two samples.

Samples	Specific Surface Area (m ² /g) ¹	Pore Volume (cm ³ /g) ²	Pore Size (nm) ³
Ru-SnTiO ₂ -P	46.807	0.185151	15.8225
Ru-SnTiO ₂ -C	37.397	0.185883	19.8823

¹ Determined from N₂ isotherm (BET method). ² Total pore volume. ³ Adsorption average pore diameter

Figure 2 presents the XRD patterns of RST-C and RST-P. The main peaks at around ~27.2°, 35.4°, and 53.7° were close to the (110), (101), and (211) planes of rutile (PDF#76-0323), indicating the dominant rutile phase in the RST catalysts. The characteristic peaks of ruthenium oxide crystals, at around 35.3° and 54.6° (PDF#88-0322), were not distinguished due to their similar peak positions with the rutile phase. It was reported that the highly dispersed RuO₂ particles smaller than 3 nm on the surface of the catalyst were formed amorphously, so the XRD peaks were not detected [14]. Comparing the two samples, it is inferred that the plasma treatment had no obvious effect on the original crystal structure. In order to determine the structural changes of these samples, the Rietveld method was conducted to refine the XRD patterns based on the Inorganic Crystal Structure Database (ICSD), and the results are presented in Table 2. In this process, Chebyshev polynomials were used to fit the background, and subsequently the pseudo-Voigt approximation of the Voigt function is used for cell refinement. There is no significant difference in cell parameters. However, RST-C attained a bigger grain size than RST-P, due to the growth of catalyst crystals at high temperatures. The low-temperature plasma treatment induced a decreased grain size, resulting in the higher specific surface area of RST-P.

Table 2. Rietveld refinement of the XRD patterns.

Samples	a(Å)	b(Å)	c(Å)	Crystalline Size (nm)
RST-P	4.6233	4.6233	2.9932	9.3
RST-C	4.6259	4.6259	2.9876	12.3

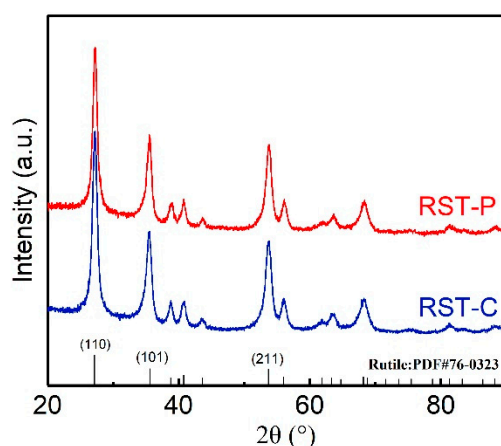


Figure 2. XRD spectra of the RST catalysts. The peak information for different crystal planes of rutile TiO_2 (No. 76-0323) is presented in figure.

Transmission electron microscopy (TEM) was employed in order to further investigate the impact of plasma treatment on the catalyst structure. TEM images of RST-C and RST-P are presented in Figure 3a,e. It is obvious that particles of RST-P possess better dispersion and smaller particle size than RST-C (the average diameter of RST-C was approximately 23 nm and that of RST-P was about 15 nm). The electrons generated by plasma were inclined to gather on the surface of the nanomaterial, which made them repel each other, avoiding the agglomeration of the particles. As shown in Figure 3b,f, the crystal of TiO_2 (110), with interplanar spacing of 0.3256 and 0.3273 nm, can be apparently observed in RST-P and RST-C, respectively. This decrease in interplanar spacing was caused by the charging process in the plasma generation process. Previous works showed that a highly charged atmosphere could force the precursors to be charged and repel from each other, which eventually causes the migration of the doping component to the surface [22], which might cause the migration of Sn in RST-P. On the other hand, the electrons formed a strong electric field on the surface of the catalyst, where RuO_2 existed in a hemispherical shape. This led to the enhancement of the interaction between RuO_2 and TiO_2 , so that the Ru was essentially getting closer to Sn- TiO_2 . To conclude, given that the radius of Sn^{4+} is larger than Ti^{4+} , while the ion radius of Ru^{4+} (0.62 nm) is greater than that of Ti^{4+} (0.53 nm), the promotion of the contact will increase the overall crystallite size of the catalyst.

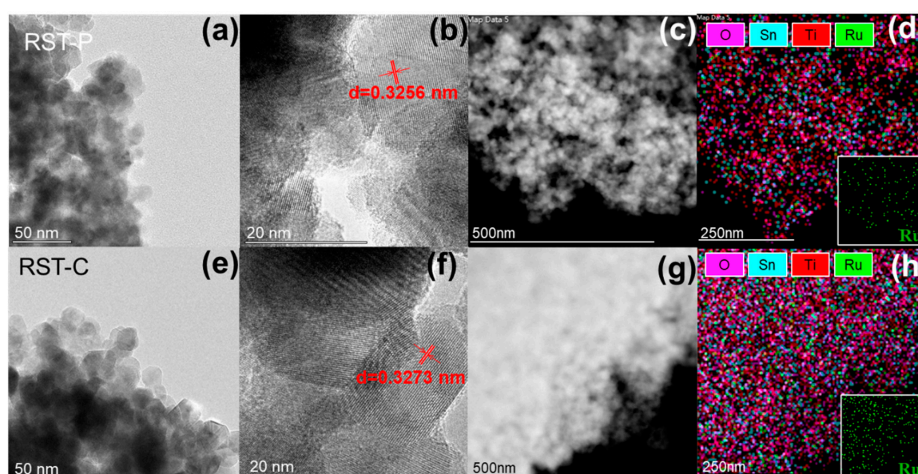


Figure 3. TEM images of (a) RST-P and (e) RST-C. The interplanar crystal spacing measured from HR-TEM images of (b) RST-P and (f) RST-C; STEM images of (c) RST-P and (g) RST-C with their EDS-mapping analysis of the RST-P (d) and RST-C (h). The distribution of Ru element is shown in the lower right corners of graphs (d,h).

The EDS mapping characterization results are shown in Figure 3d,h. These characteristics reveal that both samples attained the macroscopic homogenous distribution of Sn and Ru in the rutile matrices. According to previous studies, anatase converts into the rutile type, on which RuO_2 could epitaxially grow, with the doping of Sn [14]. This homogenous structure promoted the dispersion of RuO_2 , which was beneficial to the catalytic DCM oxidation for both samples.

2.3. Surface Properties of the Catalysts

Since catalytic reactions occurred on the catalyst surface, XPS characterization was further used to study the oxidation states of the surface Ru and oxygen species. Figure 4a indicates that the oxygen species on both samples can be divided into the three parts: surface chemisorbed oxygen (peaks at about 531.5 eV, denoted as O_{ad}), oxygen vacancies (peaks at about 531.1 eV, denoted as O_{v}) and lattice oxygen (peaks at around 528.4 eV, denoted as O_{lat}) [42,43]. The fitting results indicated that RST-P had a greater proportion of oxygen vacancies, without any loss of surface adsorption oxygen. Previous studies showed that the adsorbed oxygen species on the surface promoted the deep oxidation of the intermediate reaction species, followed by the improvement of the CO_2 selectivity [44]. Correspondingly, the oxygen vacancy was regarded as the adsorption site for DCM, and the activation of the C–Cl bond in the DCM molecules might be promoted by oxygen vacancies [45]. Meanwhile, catalysts with more oxygen vacancies after plasma treatment were more favorable for DCM oxidation, which was consistent with the characterization results of the catalytic performance.

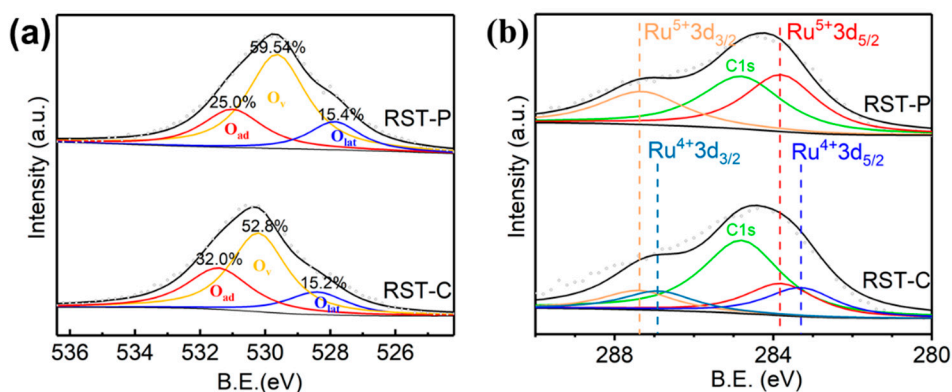


Figure 4. XPS data of (a) O 1s and (b) Ru 3d for the RST catalysts.

The distribution of surface Ru species is shown in Figure 4b. It was suggested that the peaks located at the binding energies of 283.3 eV and 286.9 eV were assigned to $\text{Ru}^{4+} 3d_{5/2}$ and $\text{Ru}^{4+} 3d_{3/2}$, respectively, while those of 283.8 eV and 287.4 eV were assigned to $\text{Ru}^{5+} 3d_{5/2}$ and $\text{Ru}^{5+} 3d_{3/2}$ [46]. After plasma modification, Ru^{5+} is the dominant oxidation state of surface Ru in RST-P compared with RST-C. It is proposed that during plasma treatment, the interaction between Ru and Sn-TiO₂ was enhanced, which means Ru transferred more electrons to Sn-TiO₂ to become more oxidized. Meanwhile, RuO_2 is highly dispersed on the surface of the rutile $\text{Sn}_{0.2}\text{Ti}_{0.8}\text{O}_2$ carrier as a result of TEM, so more RuO_2 is in direct contact with the Sn-TiO₂ via the chemical bonds formed in the plasma atmosphere, by which the electron transfer was facilitated.

The oxidation activity performance of the RST catalysts was investigated by H₂-TPR. As shown in Figure 5, the reduction peak of inner RuO_2 (139 °C) dominates the type of ruthenium oxide for RST-C. RST-P showed the main reduction peak of outer RuO_2 (97 °C), which indicated that the low-temperature redox performance of the catalysts had been significantly improved. In order to further identify the oxidation performance, the total low-temperature reduction peaks of the two RuO_2 -loaded catalysts were fitted into three peaks around 97.0 °C, 139 °C and 167 °C, which is presented in Table 3 [47]. It is worth noting that the peaks mentioned above were attributed to different forms of RuO_2 [48]. The 97 °C reduction peak was related to an easier reduction pathway, which was interpreted as the

outer RuO₂ species exposed to the gas phase, directly contacting the DCM molecules; correspondingly, the 139 °C reduction peak can be regarded as the inner RuO₂ species that required more energy as a result of the indirect contact with the gas molecules, while the 167 °C peak refers to the interfacial part of the RuO₂ particle with Sn-TiO₂.

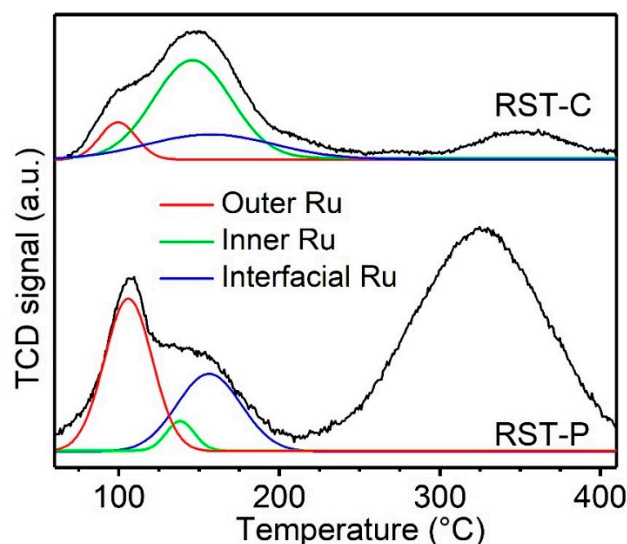


Figure 5. H₂-TPR profiles of the catalysts.

Table 3. Proportion of different peaks in H₂-TPR.

Temperature (°C)	RST-C	RST-P	Ru Species
97	13.21%	56.66%	Outer Ru
139	60.17%	10.15%	Inner Ru
167	26.61%	33.19%	Interfacial Ru

RST-P showed the dominant reduction peak at 97 °C, rather than at 139 °C, which was mainly occupied in RST-C, while the reduction peak at 167 °C became higher. This result was attributed to the decrease in RuO₂ size and the promotion of contact between RuO₂ and Sn-TiO₂ [49]. During plasma treatment, RuO₂ particles were charged and repelled from each other to get dispersed, leading to the increase in outer RuO₂ and decrease in inner RuO₂. This trend was further supported by the enhanced metallic dispersion from CO pulse chemisorption (Table 4). At the same time, the charge captured by RuO₂ enhanced the contact between RuO₂ and Sn-TiO₂, which was also expected to transform the content of the inner RuO₂ to the form of interfacial RuO₂. At the temperature of 300–400 °C, both samples displayed a broad reduction peak, which was mainly assigned to the reduction of Sn⁴⁺ species. RST-P attained a violent increase in Sn⁴⁺ reduction peak, thanks to the migration of Sn to the surface of the solid solution, which coincided with the TEM result.

Table 4. Metallic dispersion by CO pulse chemisorption.

Project	RST-C	RST-P
Metallic dispersion ¹	1.7827%	10.5071%
Metallic Surface Area(m ² /g) sample ²	0.1936	1.1412
Metallic Surface Area(m ² /g) metal ³	8.4961	50.0766

¹ The ratio of active metal atoms to the total metal atoms on the surface of catalysts. ² Surface area of Ru species per unit mass of total sample. ³ Surface area of Ru species per unit mass of Ru.

3. Discussion

During plasma treatment, the discharged atmosphere played an important role in catalyst modification. Considering the increased density of the electric charge, the charged active species mainly concentrated in the micropores of the metal oxide, which changed the microstructure of the catalyst in a physical way, and promoted the properties of the catalyst with high specific surface area and small particle size. From a chemical perspective, the highly charged atmosphere oxidized RuO_2 to a higher oxidation state, which was beneficial to the DCM oxidation. At the same time, the electric charge concentrated on RuO_2 was found to cause a high dispersion of RuO_2 . Therefore, the superior catalytic performance is mainly attributed to the discharged atmosphere generated by DBD plasma, whereby a high surface area, a good dispersion of RuO_2 and a high oxidation of Ru species were formed to help the catalyst gain a superb oxidation activity.

4. Materials and Methods

4.1. Synthesis of Ru-Sn-Ti Catalysts

4.1.1. Synthesis of $\text{Sn}_{0.2}\text{Ti}_{0.8}\text{O}_2$ Support

$\text{Sn}_{0.2}\text{Ti}_{0.8}\text{O}_2$ solid solutions were prepared via the co-precipitation method [35]; 2.77 g SnCl_4 (Macklin) was dissolved in 120 mL deionized water with stirring for 2 h. Then 14.49 g tetrabutyl titanate (TBT, Sinopharm) was added dropwise at a speed of 2 mL/min into the solution with vigorous stirring for 2 h till the suspension became uniform. We then added ammonium hydroxide (Sinopharm) with mechanical stirring controlled with the speed of 3 mL/min until the pH value reached 10. The mixture was aged overnight, washed with deionized water and ethanol 3 times each, and centrifuged to obtain the sediment. The solid product was dried at 110 °C for 12 h and subsequently calcinated at 550 °C for 5 h at a ramping rate of 10 °C/min.

4.1.2. Synthesis of $\text{RuO}_2/\text{Sn}_{0.2}\text{Ti}_{0.8}\text{O}_2$

The RuO_2 nanoparticles were prepared by first dissolving 195 mg of $\text{RuCl}_3 \cdot \text{H}_2\text{O}$ (Aladdin) in 40 mL deionized water. Then, 39 mL 15% H_2O_2 (Sigma-Aldrich) solution was added dropwise to the RuCl_3 solution with violent whisking. The mixture was stirred at 95 °C in an oil bath for 2 h and then cooled to room temperature to obtain a black suspension of RuO_2 nanoparticles. Afterwards, 5g $\text{Sn}_{0.2}\text{Ti}_{0.8}\text{O}_2$ powder was added into the above suspension until fully immersed. The solvent was evaporated and the solid was dried and ground to obtain $\text{RuO}_2/\text{Sn}_{0.2}\text{Ti}_{0.8}\text{O}_2$ (RST) precursor. The obtained solid was divided into two portions. One portion of RST precursor was treated by DBD-induced plasma atmosphere with 20% O_2 for 90 min in the discharging tube denoted as RST-P, where the air atmosphere was used to make it low-cost for catalyst preparation. The discharge parameters were determined to reach the maximum of what the reactor could withstand, and these were as follows: frequency 9 kHz, discharge voltage 10 kV and discharge power 100 W. For comparison, the other portion was calcined at 550 °C for 5 h in air (denoted as RST-C).

4.2. Material Characterizations

The X-ray diffraction patterns (XRD) of samples were collected from 10° to 90° by a Cu $\text{K}\alpha$ radiation APEXII powder diffractometer with 0.02° as the step size, presented by X-pert Powder (PANalytical B.V., Netherlands). The specific surface area was measured with an Autosorb-1-C instrument at -196.15 °C and calculated using the BET method. XPS spectra were presented by a Thermo VG ESCALAB MARK II with 1453.6 eV Mg $\text{K}\alpha$ radiation at a step of 0.2 eV, which was corrected by C1s with the binding energy of 284.8 eV. A JEOL 2100F HR-TEM/STEM microscope with X-ray energy dispersive (XEDS) spectra was employed to attain different element composition analyses and TEM images. XEDS mapping was used to analyze the distribution of different elements via an INCA x-sight (Oxford Instruments, Abingdon, United Kingdom). The specimens were prepared by

dropping the sample powder, which was dispersed in ethanol suspension, upon the perforated carbon film. CO pulse chemical adsorption was performed by using an AutoChem II 2920 instrument for CO adsorption at a low temperature. The sample was heated to 573 K in an He/Ar flow and held at this temperature for 15 min. After purging with He/Ar, the sample was reduced in 10% H₂/Ar for 15 min and then cooled to 323 K in an He/Ar flow. The catalyst oxidation was obtained using an AutoChem II 2920 (Micromeritics Instrument Corporation, Norcross, GA, USA) equipped with a thermal conductivity detector. First, pretreatment, whereby the samples were heated up to 300 °C for 1 h in helium, was performed. After purging, H₂-TPD was carried out from 30 °C to 600 °C at a rate of 10 °C/min, recorded ten times every second.

4.3. Catalytic Activity Measurements

The catalytic performance of samples was evaluated from 150 °C to 500 °C, in a quartz tube reactor of which the inner diameter was 6 mm, at a feed flow of 75 mL/min. The reactive atmosphere consisted of 1000 ppm DCM, 20% O₂ and the rest was balanced with N₂. The tested catalysts were transformed into 40–60 mesh size, and sequentially packed into the reactor. The weight hourly space velocity (WHSV) was determined to reach 45,000 mL/(g·h) when 200 mg of catalyst was added. An FT-IR gas analyzer (Gaset Dx4000, Temet Instrument Oy, Helsinki, Finland) was used to measure the concentration of DCM, CO₂, and other products in the reactor effluent. T90% was calculated by linear fitting between adjacent data points.

The chemical equation was applied accordingly:



It is expected to calculate the total conversion rate of DCM, α , and product selectivity, S, by:

$$\alpha_{\text{DCM}} = \frac{c_{\text{in}} - c_{\text{out}}}{c_{\text{in}}} \times 100\% \quad (2)$$

$$S_{\text{CO}_2} = \frac{c_{\text{CO}_2}}{c_{\text{in}} - c_{\text{out}}} \times 100\% \quad (3)$$

where c_{in} and c_{out} are the detected concentrations of DCM at the inlet and outlet, and c_{CO_2} is the concentration of CO₂ at the outlet.

5. Conclusions

DBD plasma treatment was adopted to prepare the RuO₂/Sn_{0.2}Ti_{0.8}O₂ catalyst, which showed better catalytic activity and CO₂ selectivity after plasma modification compared to the catalyst prepared by the calcination method. During the catalyst preparation, the discharge atmosphere plays a key role in modifying the catalyst and promoting catalytic performance. Non-thermal plasma allows a low temperature discharge, which prevents the growth of crystals and the agglomeration of particles in order to obtain highly specific surface area and small particle sizes. Plasma treatment also promoted the transferring of electrons from Ru to Sn-TiO₂, and sequentially pushed the oxidation from Ru⁴⁺ to Ru⁵⁺, which was expected to offer the catalyst better oxidation activity. The superior catalytic performance is mainly attributed to the high specific surface area and good dispersion of RuO₂ on the Sn-Ti support. Abundant Ru⁵⁺ species were also formed to help the catalyst gain a superb oxidation activity.

Author Contributions: Conceptualization, Y.F. and Y.Y.; methodology, Y.F. and Z.Z.; validation, X.Z., Q.X., C.Z. and X.G.; formal analysis, Y.F.; investigation, Y.F. and Y.Z. (You Zhang); resources, X.G.; data curation, S.L., Y.Z. (Yu Zhang) and X.Z.; writing—original draft preparation, Y.F.; writing—review and editing, Y.F., X.Z., and X.G.; All authors have read and agreed to the published version of the manuscript.

Funding: This work is supported by the National Key Research and Development Program of China (No. 2017YFC0210904), National Science Foundation of China (51836006, NO. U1609212).

Acknowledgments: The authors wish to thank Center of Electron Microscopy Zhejiang University for the HR-TEM experiments. Thanks are due to Lingyu Shao for assistance with the experiment and to Chang Liu for valuable discussion.

Conflicts of Interest: The authors declare no conflict of interest.

References

1. Dobrzynska, E.; Posniak, M.; Szewczynska, M.; Buszewski, B. Chlorinated Volatile Organic Compounds—Old, However, Actual Analytical and Toxicological Problem. *Crit. Rev. Anal. Chem.* **2010**, *40*, 41–57. [[CrossRef](#)]
2. Yoshikawa, M.; Zhang, M.; Toyota, K. Biodegradation of Volatile Organic Compounds and Their Effects on Biodegradability under Co-Existing Conditions. *Microbes Environ.* **2017**, *32*, 188–200. [[CrossRef](#)] [[PubMed](#)]
3. Aranzabal, A.; Pereda-Ayo, B.; Pilar Gonzalez-Marcos, M.; Gonzalez-Marcos, J.A.; Lopez-Fonseca, R.; Gonzalez-Velasco, J.R. State of the art in catalytic oxidation of chlorinated volatile organic compounds. *Chem. Pap.* **2014**, *68*, 1169–1186. [[CrossRef](#)]
4. Balasubramanian, P.; Philip, L.; Bhallamudi, S.M. Biodegradation of Chlorinated and Non-chlorinated VOCs from Pharmaceutical Industries. *Appl. Biochem. Biotechnol.* **2011**, *163*, 497–518. [[CrossRef](#)]
5. Lei, C.; Liang, F.; Li, J.; Chen, W.; Huang, B. Electrochemical reductive dechlorination of chlorinated volatile organic compounds (Cl-VOCs): Effects of molecular structure on the dehalogenation reactivity and mechanisms. *Chem. Eng. J.* **2019**, *358*, 1054–1064. [[CrossRef](#)]
6. Jin, R.; Zheng, M.; Yang, H.; Yang, L.; Wu, X.; Xu, Y.; Liu, G. Gas–particle phase partitioning and particle size distribution of chlorinated and brominated polycyclic aromatic hydrocarbons in haze. *Environ. Pollut.* **2017**, *231*, 1601–1608. [[CrossRef](#)]
7. Tsai, J.-H.; Lin, K.-H.; Chen, C.-Y.; Lai, N.; Ma, S.-Y.; Chiang, H.-L. Volatile organic compound constituents from an integrated iron and steel facility. *J. Hazard. Mater.* **2008**, *157*, 569–578. [[CrossRef](#)]
8. Mo, Z.; Shao, M.; Lu, S.; Qu, H.; Zhou, M.; Sun, J.; Gou, B. Process-specific emission characteristics of volatile organic compounds (VOCs) from petrochemical facilities in the Yangtze River Delta, China. *Sci. Total Environ.* **2015**, *533*, 422–431. [[CrossRef](#)]
9. Dai, C.; Zhou, Y.; Peng, H.; Huang, S.; Qin, P.; Zhang, J.; Yang, Y.; Luo, L.; Zhang, X. Current progress in remediation of chlorinated volatile organic compounds: A review. *J. Ind. Eng. Chem.* **2018**, *62*, 106–119. [[CrossRef](#)]
10. Li, J.-J.; Yu, E.-Q.; Cai, S.-C.; Chen, X.; Chen, J.; Jia, H.-P.; Xu, Y.-J. Noble metal free, CeO₂/LaMnO₃ hybrid achieving efficient photo-thermal catalytic decomposition of volatile organic compounds under IR light. *Appl. Catal. B Environ.* **2019**, *240*, 141–152. [[CrossRef](#)]
11. Fernández-Martínez, G.; López-Mahía, P.; Muniategui-Lorenzo, S.; Prada-Rodríguez, D.; Fernández-Fernández, E. Distribution of volatile organic compounds during the combustion process in coal-fired power stations. *Atmos. Environ.* **2001**, *35*, 5823–5831. [[CrossRef](#)]
12. Li, C.; Zhao, Y.; Song, H.; Li, H. A review on recent advances in catalytic combustion of chlorinated volatile organic compounds. *J. Chem. Technol. Biotechnol.* **2020**, *95*, 2069–2082. [[CrossRef](#)]
13. Kamal, M.S.; Razzak, S.A.; Hossain, M.M. Catalytic oxidation of volatile organic compounds (VOCs)—A review. *Atmos. Environ.* **2016**, *140*, 117–134. [[CrossRef](#)]
14. Zheng, Z.; Yang, Y.; Li, H.; Xin, Q.; Zhang, S.; Liu, Y.; Liu, S.; Zheng, C.; Song, H.; Gao, X. Effect of multi-pollutant on the catalytic oxidation of dichloromethane over RuO₂-WO₃/Sn_{0.2}Ti_{0.8}O₂ catalyst. *Fuel* **2020**, *278*, 118207. [[CrossRef](#)]
15. Deng, W.; Tang, Q.; Huang, S.; Zhang, L.; Jia, Z.; Guo, L. Low temperature catalytic combustion of chlorobenzene over cobalt based mixed oxides derived from layered double hydroxides. *Appl. Catal. B Environ.* **2020**, *278*, 119336. [[CrossRef](#)]
16. Feng, X.; Tian, M.; He, C.; Li, L.; Shi, J.-W.; Yu, Y.; Cheng, J. Yolk-shell-like mesoporous CoCrOx with superior activity and chlorine resistance in dichloromethane destruction. *Appl. Catal. B Environ.* **2020**, *264*, 118493. [[CrossRef](#)]
17. Wang, J.; Zhao, H.; Song, J.; Zhu, T.; Xu, W. Structure-Activity Relationship of Manganese Oxide Catalysts for the Catalytic Oxidation of (chloro)-VOCs. *Catalysts* **2019**, *9*, 726. [[CrossRef](#)]
18. Dai, Q.; Wu, J.; Deng, W.; Hu, J.; Wu, Q.; Guo, L.; Sun, W.; Zhan, W.; Wang, X. Comparative studies of P/CeO₂ and Ru/CeO₂ catalysts for catalytic combustion of dichloromethane: From effects of H₂O to distribution of chlorinated by-products. *Appl. Catal. B Environ.* **2019**, *249*, 9–18. [[CrossRef](#)]

19. Li, N.; Cheng, J.; Xing, X.; Sun, Y.; Hao, Z. Distribution and formation mechanisms of polychlorinated organic by-products upon the catalytic oxidation of 1,2-dichlorobenzene with palladium-loaded catalysts. *J. Hazard. Mater.* **2020**, *393*, 122412. [[CrossRef](#)]
20. Zhang, L.; Liu, X.; Scurrell, M.S. Cold plasmas in the modification of catalysts. *Rev. Chem. Eng.* **2018**, *34*, 201–213. [[CrossRef](#)]
21. Tang, X.; Li, K.; Yi, H.; Ning, P.; Xiang, Y.; Wang, J.; Wang, C. MnOx Catalysts Modified By Nonthermal Plasma For NO Catalytic Oxidation. *J. Phys. Chem. C* **2012**, *116*, 10017–10028. [[CrossRef](#)]
22. Liu, C.-J.; Vissokov, G.P.; Jang, B.W.L. Catalyst preparation using plasma technologies. *Catal. Today* **2002**, *72*, 173–184. [[CrossRef](#)]
23. Duan, Z.; Du, G. Research Advances on Wood Material Modification by Plasma Treatment. *World For. Res.* **2017**, *30*, 51–55.
24. Gao, Y.; Jiang, W.; Luan, T.; Li, H.; Zhang, W.; Feng, W.; Jiang, H. High-Efficiency Catalytic Conversion of NOx by the Synergy of Nanocatalyst and Plasma: Effect of Mn-Based Bimetallic Active Species. *Catalysts* **2019**, *9*, 103. [[CrossRef](#)]
25. Chen, B.; Wang, B.; Sun, Y.; Wang, X.; Fu, M.; Wu, J.; Chen, L.; Tan, Y.; Ye, D. Plasma-Assisted Surface Interactions of Pt/CeO₂ Catalyst for Enhanced Toluene Catalytic Oxidation. *Catalysts* **2019**, *9*, 2. [[CrossRef](#)]
26. Aluha, J.; Hu, Y.; Abatzoglou, N. Effect of CO Concentration on the alpha-Value of Plasma-Synthesized Co/C Catalyst in Fischer-Tropsch Synthesis. *Catalysts* **2017**, *7*, 69. [[CrossRef](#)]
27. Zhao, B.; Yao, Y.; Shi, H.; Yang, F.; Jia, X.; Liu, P.; Ma, X. Preparation of Ni/SiO₂ catalyst via novel plasma-induced micro-combustion method. *Catal. Today* **2019**, *337*, 28–36. [[CrossRef](#)]
28. Herrmann, I.; Brüser, V.; Fiechter, S.; Kersten, H.; Bogdanoff, P. Electrocatalysts for Oxygen Reduction Prepared by Plasma Treatment of Carbon-Supported Cobalt Tetramethoxyphenylporphyrin. *J. Electrochem. Soc.* **2005**, *152*, A2179. [[CrossRef](#)]
29. Derikvandi, H.; Nezamzadeh-Ejhi, A. Increased photocatalytic activity of NiO and ZnO in photodegradation of a model drug aqueous solution: Effect of coupling, supporting, particles size and calcination temperature. *J. Hazard. Mater.* **2017**, *321*, 629–638. [[CrossRef](#)]
30. Pham Van, T.; Le Trung, H.; Chu Manh, H.; Hoang Ba, T.; Vu Thi, T.; Tran Thi Quynh, H.; Nguyen Xuan, S.; Tran Ngoc, K. Effects of annealing temperature on the structure, morphology, and photocatalytic properties of SnO₂/rGO nanocomposites. *Nanotechnology* **2020**, *32*, 015201. [[CrossRef](#)]
31. Bian, Y.; Wang, X.; Hu, Z. Synthesis of mesoporous titania thin films by a simple route at low-temperature via plasma treatment. *J. Mater. Sci.* **2013**, *48*, 4088–4096. [[CrossRef](#)]
32. Mokhtar, M.; Alhashedi, B.F.A.; Kashmery, H.A.; Ahmed, N.S.; Saleh, T.S.; Narasimharao, K. Highly Efficient Nanosized Mesoporous CuMgAl Ternary Oxide Catalyst for Nitro-Alcohol Synthesis: Ultrasound-Assisted Sustainable Green Perspective for the Henry Reaction. *ACS Omega* **2020**, *5*, 6532–6544. [[CrossRef](#)]
33. Fujishima, A.; Zhang, X.; Tryk, D.A. TiO₂ photocatalysis and related surface phenomena. *Surf. Sci. Rep.* **2008**, *63*, 515–582. [[CrossRef](#)]
34. Noman, M.T.; Ashraf, M.A.; Ali, A. Synthesis and applications of nano-TiO₂: A review. *Environ. Sci. Pollut. Res.* **2019**, *26*, 3262–3291. [[CrossRef](#)]
35. Yang, Y.; Li, H.; Zhao, H.; Qu, R.; Zhang, S.; Hu, W.; Yu, X.; Zhu, X.; Liu, S.; Zheng, C.; et al. Structure and crystal phase transition effect of Sn doping on anatase TiO₂ for dichloromethane decomposition. *J. Hazard. Mater.* **2019**, *371*, 156–164. [[CrossRef](#)]
36. Weng, X.; Xue, Y.; Chen, J.; Meng, Q.; Wu, Z. Elimination of chloroaromatic congeners on a commercial V₂O₅-WO₃/TiO₂ catalyst: The effect of heavy metal Pb. *J. Hazard. Mater.* **2020**, *387*, 121705. [[CrossRef](#)]
37. Liu, Y.; Johnson, N.W.; Liu, C.; Chen, R.; Zhong, M.; Dong, Y.; Mahendra, S. Mechanisms of 1,4-Dioxane Biodegradation and Adsorption by Bio-Zeolite in the Presence of Chlorinated Solvents: Experimental and Molecular Dynamics Simulation Studies. *Environ. Sci. Technol.* **2019**, *53*, 14538–14547. [[CrossRef](#)]
38. Weng, X.; Sun, P.; Long, Y.; Meng, Q.; Wu, Z. Catalytic Oxidation of Chlorobenzene over MnxCe1-xO₂/HZSM-5 Catalysts: A Study with Practical Implications. *Environ. Sci. Technol.* **2017**, *51*, 8057–8066. [[CrossRef](#)]
39. Lin, F.; Zhang, Z.; Li, N.; Yan, B.; He, C.; Hao, Z.; Chen, G. How to achieve complete elimination of Cl-VOCs: A critical review on byproducts formation and inhibition strategies during catalytic oxidation. *Chem. Eng. J.* **2021**, *404*, 126534. [[CrossRef](#)]
40. Zhang, Y.; Wang, H.-y.; Zhang, Y.-R.; Bogaerts, A. Formation of microdischarges inside a mesoporous catalyst in dielectric barrier discharge plasmas. *Plasma Sources Sci. Technol.* **2017**, *26*, 054002. [[CrossRef](#)]

41. Zhang, Y.-R.; Neyts, E.C.; Bogaerts, A. Influence of the Material Dielectric Constant on Plasma Generation inside Catalyst Pores. *J. Phys. Chem. C* **2016**, *120*, 25923–25934. [[CrossRef](#)]
42. Merino, N.A.; Barbero, B.P.; Eloy, P.; Cadús, L.E. $\text{La}_{1-x}\text{Ca}_x\text{CoO}_3$ perovskite-type oxides: Identification of the surface oxygen species by XPS. *Appl. Surf. Sci.* **2006**, *253*, 1489–1493. [[CrossRef](#)]
43. Li, Q.; Zhu, X.; Yang, J.; Yu, Q.; Zhu, X.; Chu, J.; Du, Y.; Wang, C.; Hua, Y.; Li, H.; et al. Plasma treated Bi_2WO_6 ultrathin nanosheets with oxygen vacancies for improved photocatalytic CO_2 reduction. *Inorg. Chem. Front.* **2020**, *7*, 597–602. [[CrossRef](#)]
44. Tian, M.; He, C.; Yu, Y.; Pan, H.; Smith, L.; Jiang, Z.; Gao, N.; Jian, Y.; Hao, Z.; Zhu, Q. Catalytic oxidation of 1,2-dichloroethane over three-dimensional ordered meso-macroporous $\text{Co}_3\text{O}_4/\text{La}_{0.7}\text{Sr}_{0.3}\text{Fe}_{0.5}\text{Co}_{0.5}\text{O}_3$: Destruction route and mechanism. *Appl. Catal. A Gen.* **2018**, *553*, 1–14. [[CrossRef](#)]
45. Shi, Z.; Yang, P.; Tao, F.; Zhou, R. New insight into the structure of $\text{CeO}_2\text{-TiO}_2$ mixed oxides and their excellent catalytic performances for 1,2-dichloroethane oxidation. *Chem. Eng. J.* **2016**, *295*, 99–108. [[CrossRef](#)]
46. Nong, S.; Dong, W.; Yin, J.; Dong, B.; Lu, Y.; Yuan, X.; Wang, X.; Bu, K.; Chen, M.; Jiang, S.; et al. Well-Dispersed Ruthenium in Mesoporous Crystal TiO_2 as an Advanced Electrocatalyst for Hydrogen Evolution Reaction. *J. Am. Chem. Soc.* **2018**, *140*, 5719–5727. [[CrossRef](#)]
47. Yu, J.; Zhao, D.; Xu, X.; Wang, X.; Zhang, N. Study on $\text{RuO}_2/\text{SnO}_2$: Novel and Active Catalysts for CO and CH_4 Oxidation. *ChemCatChem* **2012**, *4*, 1122–1132. [[CrossRef](#)]
48. Liu, L.; Liu, Y.; Song, J.; Ahmad, S.; Liang, J.; Sun, Y. Plasma-enhanced steam reforming of different model tar compounds over Ni-based fusion catalysts. *J. Hazard. Mater.* **2019**, *377*, 24–33. [[CrossRef](#)]
49. Li, Y.; Jang, B.W.L. Non-thermal RF plasma effects on surface properties of Pd/TiO_2 catalysts for selective hydrogenation of acetylene. *Appl. Catal. A Gen.* **2011**, *392*, 173–179. [[CrossRef](#)]

Publisher's Note: MDPI stays neutral with regard to jurisdictional claims in published maps and institutional affiliations.



© 2020 by the authors. Licensee MDPI, Basel, Switzerland. This article is an open access article distributed under the terms and conditions of the Creative Commons Attribution (CC BY) license (<http://creativecommons.org/licenses/by/4.0/>).